

Penetration depth of Ba_{1-x}K_xFe₂As₂ single crystals explained within a multiband Eliashberg s_{\pm} approach

Original

Penetration depth of Ba_{1-x}K_xFe₂As₂ single crystals explained within a multiband Eliashberg s_{\pm} approach / Ghigo, Gianluca; Ummarino, Giovanni; Gozzelino, Laura; Tamegai, T.. - In: PHYSICAL REVIEW. B. - ISSN 2469-9950. - STAMPA. - 96:1(2017), pp. 014501-1-014501-8. [[10.1103/PhysRevB.96.014501](https://doi.org/10.1103/PhysRevB.96.014501)]

Availability:

This version is available at: [11583/2677738](https://doi.org/10.11583/2677738) since: 2017-07-28T17:59:21Z

Publisher:

The American Physical Society through the American Institute of Physics

Published

DOI:[10.1103/PhysRevB.96.014501](https://doi.org/10.1103/PhysRevB.96.014501)

Terms of use:

This article is made available under terms and conditions as specified in the corresponding bibliographic description in the repository

Publisher copyright

(Article begins on next page)

Penetration depth of $\text{Ba}_{1-x}\text{K}_x\text{Fe}_2\text{As}_2$ single crystals explained within a multiband Eliashberg $s\pm$ approach

G. Ghigo,^{1,2,*} G. A. Ummarino,^{1,3} L. Gozzelino,^{1,2} and T. Tamegai⁴¹*Politecnico di Torino, Department of Applied Science and Technology, 10129 Torino, Italy*²*Istituto Nazionale di Fisica Nucleare, Sezione Torino, 10125 Torino, Italy*³*National Research Nuclear University MEPhI (Moscow Engineering Physics Institute), Moskva 115409, Russia*⁴*The University of Tokyo, Department of Applied Physics, Hongo, Bunkyo-ku, Tokyo 113-8656, Japan*

(Received 10 May 2017; published 5 July 2017)

We investigate the penetration depth of high-quality $\text{Ba}_{1-x}\text{K}_x\text{Fe}_2\text{As}_2$ single crystals by a planar waveguide resonator technique, in a cavity perturbation approach. The experimental λ_L is compared to calculations based on the three-band Eliashberg equations within the $s\pm$ wave model. To this end, the anisotropy of the penetration depth is taken into account. In fact, the agreement between theory and experiment is remarkable. The low-temperature value of the in-plane penetration depth, $\lambda_{L,ab}(5\text{ K}) = 220\text{ nm}$, and the total plasma frequency, $\omega_p = 1.0\text{ eV}$, are also consistent with earlier results. This overall consistency validates the model itself, thus allowing us to estimate parameters that are missing in literature, such as the plasma frequency for each band: it turns out that $\omega_{p,1} = \omega_{p,3} = 0.32\text{ eV}$ and $\omega_{p,2} = 0.89\text{ eV}$, with the subscripts 1 and 2 denoting the two hole bands and 3 the equivalent electron band.

DOI: [10.1103/PhysRevB.96.014501](https://doi.org/10.1103/PhysRevB.96.014501)

I. INTRODUCTION

Since their discovery, the interest in iron-based superconductors (IBS) was driven—from a fundamental point of view—by the combination of the high transition temperature, the proximity to a magnetic state, and the existence of multiple conducting bands. In fact, the number of superconducting energy gaps and their symmetry has always been among the most discussed issues [1,2].

Electron-doped and hole-doped BaFe_2As_2 compounds are among the most intensively studied systems of IBS families [3–12]. Hole doping can be achieved by partially substituting potassium for barium, $\text{Ba}_{1-x}\text{K}_x\text{Fe}_2\text{As}_2$, thus reaching a critical temperature of about 38 K for optimal doping. Most parameters of this compound are known, and a candidate for the pairing symmetry was identified in the $s\pm$ wave model [13,14]. According to this model, the interband coupling between hole and electron bands is provided by antiferromagnetic spin fluctuations. For the sake of completeness, it should be considered that another unconventional mechanism has been put forth for IBS, i.e., the orbital fluctuations, which favors the s^{++} state without sign reversal [15]. Actually, it is sometimes difficult to distinguish between the s^{++} wave and $s\pm$ wave states by experiment [16]. The initial argument against $s\pm$ wave (and in favor of s^{++}), that the observed suppression of the critical temperature by nonmagnetic impurities is much weaker than expected for a sign-changing order parameter, is not decisive. As a matter of fact, it was shown that this and other nontrivial impurity effects can be well explained within the $s\pm$ scenario, when an adequate multiband model is adopted [17,18]. To date, the $s\pm$ wave model is considered the leading candidate for describing the pairing state in most of the IBS, including $\text{Ba}_{1-x}\text{K}_x\text{Fe}_2\text{As}_2$.

To gain further insight into the fundamental mechanisms of superconductivity in these compounds, a theoretical model is needed that is simple enough to enable a quantitative comparison with experimental data but still captures the essential physics of the material. There is evidence that at least three bands are required to satisfactorily describe the physical properties of BaFeAs -based compounds [19]. The electronic structure of $\text{Ba}_{1-x}\text{K}_x\text{Fe}_2\text{As}_2$ can be approximately described by two hole bands α, β and one equivalent electron band γ [20]. As mentioned, according to the $s\pm$ wave model, the interband coupling between hole and electron bands is mainly provided by antiferromagnetic spin fluctuations, while phonons are responsible for the intraband coupling [13]. Calculations based on this simplified model should be compared to the experimental determination of parameters such as the London penetration depth, λ_L , that determines the superfluid density ρ_s , i.e., the fraction of electrons in the superconducting phase. In fact, the temperature dependence of the superfluid density is very sensitive to the detailed behavior of the energy gaps.

In this paper we investigate the penetration depth of high-quality $\text{Ba}_{1-x}\text{K}_x\text{Fe}_2\text{As}_2$ single crystals. The experimental λ_L is compared to calculations based on the three-band Eliashberg equations within the $s\pm$ wave model, in order to validate the model itself and to estimate useful parameters that are missing in literature, such as the plasma frequency for each band. To this end, also the anisotropy of the penetration depth is accounted for.

To experimentally determine the penetration depth and to characterize the high-frequency properties of the crystals, we make use of a superconducting coplanar waveguide (CPW) resonator technique, in a cavity perturbation approach. A similar approach was originally employed to characterize superconducting crystals in cylindrical cavities [21], but the small size of high-quality crystals limits the sensitivity of cavity perturbation in the large and bulky cylindrical resonators operating in the 1–10 GHz range. A cavity perturbation technique using superconducting split-ring resonators, more

*gianluca.ghigo@polito.it

compact and with improved sensitivity, was also developed [22,23]. Due to the very small dimensions of our samples (even smaller than $5 \times 10^{-4} \text{ mm}^3$, with thickness around $10 \text{ }\mu\text{m}$), we exploit the small uniformity region of planar superconducting resonators. The main advantages of such planar structures, which are practical for exploring the frequency range 1–10 GHz, are small dimensions, simple fabrication, and easy scalability. In fact, the lower value of the quality factor with respect to three-dimensional cavities is compensated by the high sensitivity to very small samples.

The paper is organized as follows. Section II contains the details about the experimental technique: samples, measurement setup, data analysis, and results. In Sec. III, the theoretical model is introduced and described. The comparison between the experimental results and the model calculations is discussed in Sec. IV, where also conclusions are drawn.

II. EXPERIMENTAL TECHNIQUE AND RESULTS

A. Samples and measurement setup

High-quality $\text{Ba}_{1-x}\text{K}_x\text{Fe}_2\text{As}_2$ crystals with an analyzed doping level of $x = 0.42$ and a critical temperature $T_c \approx 38 \text{ K}$ were grown by the FeAs self-flux method [24]. All the investigated crystals were cleaved to be thin plates with thickness ($2c$) of the order of $10 \text{ }\mu\text{m}$, more than ten times smaller than width ($2a$) and length ($2b$). The CPW resonator used for measurements consists of a patterned $\text{YBa}_2\text{Cu}_3\text{O}_{7-x}$ film with a thickness of $t = 250 \text{ nm}$, grown on an MgO substrate. Its critical temperature is of about 88 K , and the zero-temperature penetration depth was evaluated to be 155 nm [25]. The central conductor strip has a width of $w = 350 \text{ }\mu\text{m}$ and the distance between the ground planes is $d = 650 \text{ }\mu\text{m}$. Resonance frequency, f_0 (about 7.95 GHz), and unloaded quality factor, Q_0 , are evaluated from measurements of the resonance curves obtained in a Cryomech PT 415 pulse tube cooler by means of a Rohde Schwarz ZVK vector network analyzer for an input power of -40 dBm , well below the nonlinearity threshold for the resonator.

B. Use of a coplanar resonator for a cavity-perturbation analysis

The measurement is based on the exploitation of a region where rf fields are quite uniform, above the resonator. In fact, in a coplanar resonator rf currents show strong peaks at the edges: the microwave current density distribution across the center conductor can be expressed as [26]

$$j^{rf}(x) = \frac{I_{\text{tot}}}{K\left(\frac{w}{d}\right)w\sqrt{\zeta(x)}}, \quad (1)$$

where

$$\zeta(x) = \begin{cases} \frac{\lambda_{\text{eff}}}{w} \left[1 - \left(\frac{w}{d}\right)^2\right], & 0 \leq \frac{w}{2} - |x| < \lambda_{\text{eff}}, \\ \left[1 - \left(\frac{2x}{w}\right)^2\right] \left[1 - \left(\frac{2x}{d}\right)^2\right], & |x| < \frac{w}{2} - \lambda_{\text{eff}}. \end{cases}$$

I_{tot} is the total current, $\lambda_{\text{eff}} = \lambda_L \coth(t/2\lambda_L)$ is the effective penetration depth, λ_L is the London penetration depth, K is

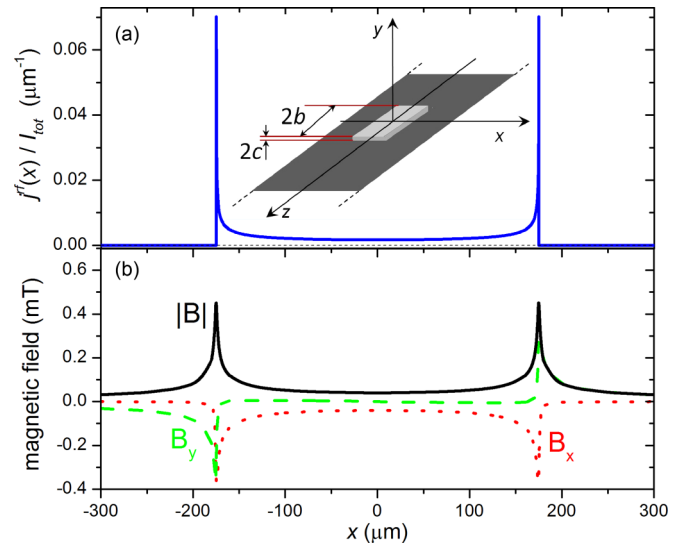


FIG. 1. (a) (Upper frame) Current density distribution across the center conductor of the coplanar line. The inset shows the reference system (origin in the resonator center) as well as the crystal position and dimensions (not to scale). (b) (Lower frame) Components and magnitude of the magnetic field as a function of the transverse position x , generated above the resonator surface ($y = 1 \text{ }\mu\text{m}$) by the rf currents flowing in the z direction. The curves were computed for a resonator with width $w = 350 \text{ }\mu\text{m}$, thickness $t = 250 \text{ nm}$, distance between ground planes $d = 650 \text{ }\mu\text{m}$, and for the measured values of $\lambda_L = 155 \text{ nm}$ and $I_{\text{tot}} = 39 \text{ mA}$.

the complete elliptic integral, and x is the coordinate along the transverse direction. Moreover, the standing wave at resonance shows nodes at the edges in the longitudinal direction (z axis) and a maximum in the resonator center. If the geometry of our resonator is considered, the current density distribution shown in Fig. 1 is obtained. This distribution of currents can be used in the Biot-Savart law to obtain the magnitude of the rf magnetic field as a function of the transverse position x , generated at a given distance above the resonator surface [Fig. 1]. There is a small region in the central part of the resonator, far from edges, where the magnetic field generated at resonance is uniform enough (within about 5%) for the purpose of deducing quantitative information about the diamagnetic and dissipative properties of a crystal coupled to the resonator, according to the procedure described below. In fact, measurements as a function of the input power show that the main measured parameters are not significantly sensitive to the amplitude of the probing rf field, allowing us to conclude that the technique is reliable—for uniform samples—even in the presence of such nonuniformity of the field [27]. The sample under test is positioned onto the resonator by a small amount of high-vacuum grease and measurements of the resonance curve are repeated in the same conditions, with and without the crystal.

C. Data analysis

When a crystal is placed in the region of homogeneous magnetic field of the microwave resonator with the broad face parallel to the field, the perturbations relative to no sample in

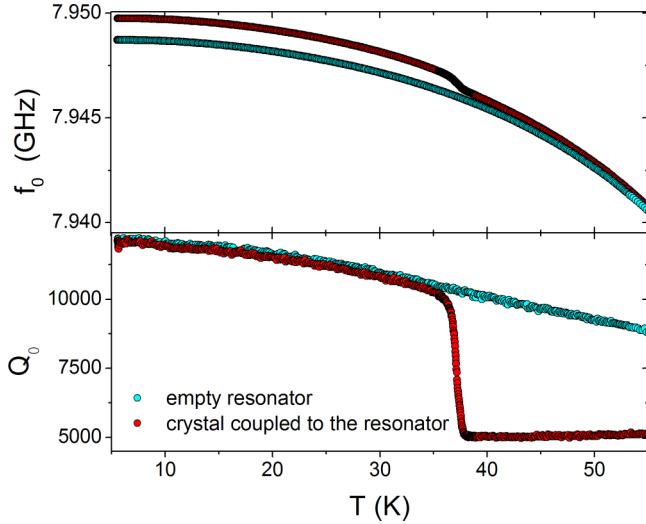


FIG. 2. Resonance frequency (upper frame) and unloaded quality factor (lower frame) as a function of temperature, for the empty resonator and in the presence of a $\text{Ba}_{1-x}\text{K}_x\text{Fe}_2\text{As}_2$ crystal.

the cavity, in terms of resonance frequency fractional shift and quality factor modification, are [28]

$$\frac{\Delta f_0}{f_0} = \frac{1}{2} \frac{V_s}{V_r} \left\{ 1 - \text{Re} \left[\frac{\tanh(kc)}{kc} \right] \right\}, \quad (2)$$

$$\Delta \left(\frac{1}{Q_0} \right) = \frac{V_s}{V_r} \text{Im} \left[\frac{\tanh(kc)}{kc} \right], \quad (3)$$

where k is the complex propagation constant and c is the crystal half-thickness. Here V_s is the volume of the sample and V_r is the effective volume of the resonator. Figure 2 shows how the resonance frequency and the unloaded quality factor are affected by the presence of the crystal.

The geometrical factor (V_s/V_r) cannot be calculated with the needed precision, especially for the open planar geometry of our resonator; rather it should be determined in a self-consistent way from data above T_c , where the crystals show a metallic behavior. For a metal $\text{Re}(k) = \text{Im}(k) = 1/\delta$, where $\delta = \sqrt{2/\omega\mu\sigma}$ is the classical skin depth. This, in combination with Eqs. (2) and (3), gives for the case of infinitely large crystals

$$2 \frac{\Delta f_0}{f_0} = \frac{V_s}{V_r} [1 - A(c)],$$

$$\Delta \left(\frac{1}{Q_0} \right) = \frac{V_s}{V_r} B(c),$$

where

$$A(x) = \frac{\delta}{2x} \frac{\sinh(\frac{2x}{\delta}) + \sin(\frac{2x}{\delta})}{\cosh(\frac{2x}{\delta}) + \cos(\frac{2x}{\delta})},$$

$$B(x) = \frac{\delta}{2x} \frac{\sinh(\frac{2x}{\delta}) - \sin(\frac{2x}{\delta})}{\cosh(\frac{2x}{\delta}) + \cos(\frac{2x}{\delta})}.$$

If the finite dimensions of the crystal are considered, the penetration of the field also from the lateral sides has to be taken into account. In our case the correction is of the order of

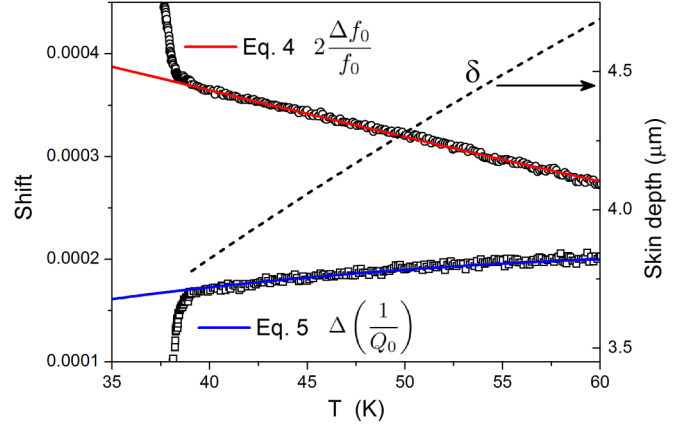


FIG. 3. Shifts of the resonance frequency and of the inverse of the quality factor as a function of temperature above T_c , induced by the presence of a $\text{Ba}_{1-x}\text{K}_x\text{Fe}_2\text{As}_2$ crystal (symbols). Experimental data are fitted by means of Eqs. (4) and (5) (solid lines), keeping the same $\delta(T)$ for both (dotted line, right scale).

few percent and the equations become

$$2 \frac{\Delta f_0}{f_0} = \frac{V_s}{V_r} [1 - A(a) - A(b) - A(c)], \quad (4)$$

$$\Delta \left(\frac{1}{Q_0} \right) = \frac{V_s}{V_r} [B(a) + B(b) + B(c)]. \quad (5)$$

For such small crystals, it can be assumed that above T_c the temperature dependence of the shifts of both resonance frequency and quality factor is mainly due to the temperature dependence of the skin depth, and the small contribution given by the thermal expansion of the sample can be neglected. Figure 3 shows the experimental f_0 and Q_0 shifts fitted by Eqs. (4) and (5), respectively, with the constraint to keep the same $\delta(T)$ for both (right scale). The resulting geometrical factors in the two cases slightly differ from each other (within 20%), reflecting the fact that systematic errors affect the f_0 and Q_0 data differently [29]. Now, Eqs. (2) and (3) allow obtaining the real and imaginary parts of the propagation constant k in the superconducting state, that are related to the magnetic penetration depth and to the normal conductivity (the correction accounting for the penetration of the field from the lateral sides can be made in this case *ex post*, and will be discussed below). On the basis of data taken from literature for this compound and doping level ($\lambda_{ab} \approx 200$ nm [30]; coherence length $\xi_{ab} \approx 0.9\text{--}1.4$ nm [20,31]; mean free path $\ell \approx 15$ nm [4]) we assume that the system is in the clean local limit. Thus the magnetic penetration depth directly extracted from measurements is assumed to be the London penetration depth, λ_L .

For a superconductor at low temperature $\text{Re}(k) \approx 1/\lambda_L$ and $\text{Im}(k) \approx 0$, if losses are negligible. If losses are not negligible, then the following expression for k is more appropriate [33]:

$$k = \left(\frac{1}{\lambda_L^2} + i\omega\mu_0\sigma_n \right)^{\frac{1}{2}}, \quad (6)$$

where σ_n is the temperature dependent normal conductivity, due to the thermally excited normal charge carriers, in the frame of a two-fluid model. Thus, λ_L and σ_n can be obtained from the real and imaginary parts of k , according to Eq. (6).

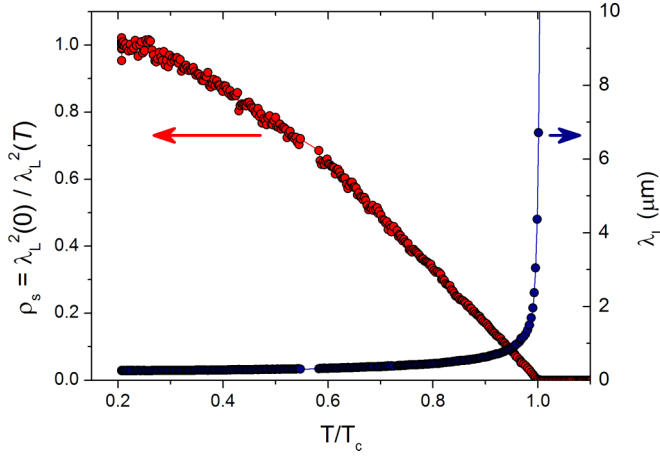


FIG. 4. London penetration depth (right scale) and superfluid density (left scale), as a function of the reduced temperature T/T_c .

Finally, the complex surface impedance, Z_s , can be calculated starting from the general expression valid for a bulk sample [26]:

$$Z_s = R_s + iX_s = \frac{i\omega\mu_0\lambda_L}{\sqrt{1 + i\omega\mu_0\sigma_n\lambda_L^2}}. \quad (7)$$

D. London penetration depth and superfluid density

Typical results of the procedure described above are presented here. Figure 4 shows the penetration depth and the superfluid density evaluated as $\rho_s(T) = \lambda_L^2(0)/\lambda_L^2(T)$ as a function of reduced temperature, and Fig. 5 shows the real and imaginary parts of the surface impedance.

Correctly, $\lambda_L(T)$ diverges at T_c , where the microwave λ connects to the skin depth δ . At low temperatures, the values of the penetration depth measured for different crystals are in the range $\lambda_L(T) = 200\text{--}240$ nm. Such a spread is due not only to experimental errors, but also to the anisotropy of the penetration depth: the measured penetration depth is a combination of an in-plane component $\lambda_{L,ab}$ and an out-of-plane component $\lambda_{L,c}$. The way these two components

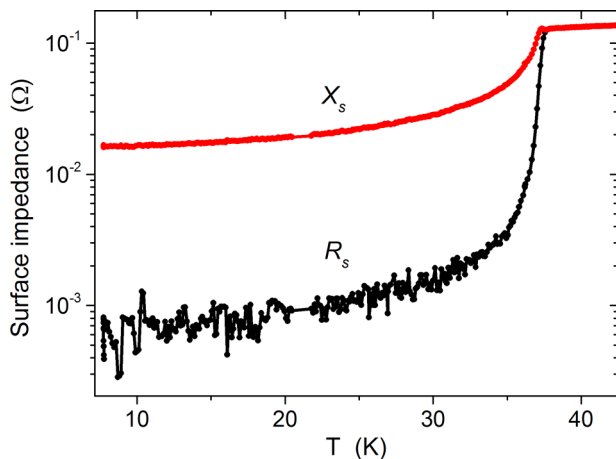


FIG. 5. Real (R_s) and imaginary part (X_s) of the surface impedance of a $\text{Ba}_{1-x}\text{K}_x\text{Fe}_2\text{As}_2$ crystal.

are combined depends on the geometry of the crystal, as will be discussed in Sec. IV.

It has been pointed out many times in literature (see for example Ref. [30]) that attempts to fit the experimental $\rho_s(T)$ curves such as the one reported in Fig. 4 in a standard single-gap scheme cannot be successful. Therefore, a multigap calculation is proposed in the following section.

III. THE MODEL

A. Introduction

As stated in the Introduction, the electronic structure of the compound $\text{Ba}_{1-x}\text{K}_x\text{Fe}_2\text{As}_2$ can be approximately described by a three-band model with two hole bands α , β (indicated in the following as bands 1 and 2) and one equivalent electron band γ (indicated in the following as band 3) [20]. Within the $s\pm$ wave model, due to the antiferromagnetic spin fluctuation coupling between the electron and the hole bands, the gap of the electron band, Δ_3 , has opposite sign with respect to the gaps residing on the hole bands, Δ_1 and Δ_2 [13].

The first aim of calculations is to reproduce the correct values of the gaps and of the critical temperature. Reference values for the gaps were set on the basis of angle-resolved photoelectron spectroscopy (ARPES) experiments in single crystals of the same compound, with the same doping level and similar T_c [20,34–38]: $\Delta_1 = 12.1 \pm 1$ meV, $\Delta_2 = 5.2 \pm 1.0$ meV, and $|\Delta_3| = 12.8 \pm 1.4$ meV. The gaps in $\text{Ba}_{1-x}\text{K}_x\text{Fe}_2\text{As}_2$ were also investigated by other experimental techniques, e.g., muon spin relaxation, nuclear magnetic resonance, and specific heat [32,39–43], but not always was a three-band analysis performed, and/or the doping level of the samples was not exactly the same as investigated here. To calculate the gaps and the critical temperature within the $s\pm$ wave three-band Eliashberg equations [44,45], one has to solve six coupled equations for the gaps $\Delta_i(i\omega_n)$ and the renormalization functions $Z_i(i\omega_n)$, where i is the band index (ranging from 1 to 3) and ω_n are the Matsubara frequencies. The imaginary-axis equations read [46–48]:

$$\omega_n Z_i(i\omega_n) = \omega_n + \pi T \sum_{m,j} \Lambda_{ij}^Z(i\omega_n, i\omega_m) N_j^Z(i\omega_m) + \sum_j [\Gamma_{ij}^N + \Gamma_{ij}^M] N_j^Z(i\omega_n), \quad (8)$$

$$Z_i(i\omega_n) \Delta_i(i\omega_n) = \pi T \sum_{m,j} [\Lambda_{ij}^\Delta(i\omega_n, i\omega_m) - \mu_{ij}^*(\omega_c)] \times \Theta(\omega_c - |\omega_m|) N_j^\Delta(i\omega_m) + \sum_j j [\Gamma_{ij}^N + \Gamma_{ij}^M] N_j^\Delta(i\omega_n), \quad (9)$$

where Γ_{ij}^N and Γ_{ij}^M are the scattering rates from nonmagnetic and magnetic impurities, $\Lambda_{ij}^Z(i\omega_n, i\omega_m) = \Lambda_{ij}^{ph}(i\omega_n, i\omega_m) + \Lambda_{ij}^{sf}(i\omega_n, i\omega_m)$ and $\Lambda_{ij}^\Delta(i\omega_n, i\omega_m) = \Lambda_{ij}^{ph}(i\omega_n, i\omega_m) - \Lambda_{ij}^{sf}(i\omega_n, i\omega_m)$, where

$$\Lambda_{ij}^{ph,sf}(i\omega_n, i\omega_m) = 2 \int_0^{+\infty} d\Omega \Omega \alpha_{ij}^2 F^{ph,sf}(\Omega) / [(\omega_n - \omega_m)^2 + \Omega^2].$$

Θ is the Heaviside function and ω_c is a cutoff energy. The quantities $\mu_{ij}^*(\omega_c)$ are the elements of the 3×3 Coulomb pseudopotential matrix. Finally, $N_j^A(i\omega_m) = \Delta_j(i\omega_m)/\sqrt{\omega_m^2 + \Delta_j^2(i\omega_m)}$ and $N_j^Z(i\omega_m) = \omega_m/\sqrt{\omega_m^2 + \Delta_j^2(i\omega_m)}$. The electron-boson coupling constants are defined as $\lambda_{ij}^{ph, sf} = 2 \int_0^{+\infty} d\Omega \frac{\alpha_{ij}^2 F^{ph, sf}(\Omega)}{\Omega}$.

The solution of Eqs. (8) and (9) requires a huge number of input parameters: (i) nine electron-phonon spectral functions $\alpha_{ij}^2 F^{ph}(\Omega)$; (ii) nine electron-antiferromagnetic spin fluctuations spectral functions, $\alpha_{ij}^2 F^{sf}(\Omega)$; (iii) nine elements of the Coulomb pseudopotential matrix $\mu_{ij}^*(\omega_c)$; (iv) nine non-magnetic Γ_{ij}^N and nine paramagnetic Γ_{ij}^M impurity-scattering rates. However, some of these parameters can be extracted from experiments and some others can be fixed by suitable approximations. In particular, we refer to experimental data taken in single crystals of high quality, so we can rather safely assume a negligible disorder; the scattering from nonmagnetic impurities Γ_{ij}^N can thus be taken to be zero. The same can be done for the scattering rate from magnetic impurities: $\Gamma_{ij}^M = 0$. At least as a starting point, let us make further assumptions that have been shown to be valid for iron pnictides [46–48]. Following Ref. [13], we can assume that (i) the total electron-phonon coupling constant is small (the upper limit of the phonon coupling in the usual iron-arsenide compounds is ≈ 0.35) [49]; (ii) phonons mainly provide *intraband* coupling so that $\lambda_{ij}^{ph} \approx 0$; (iii) spin fluctuations mainly provide *interband coupling between holes and electrons bands*, so that $\lambda_{ii}^{sf} \approx 0$. Moreover, in first approximation the phonon contribution to *intraband* coupling is negligible so that $\lambda_{ii}^{ph} = 0$, and the same for the Coulomb pseudopotential matrix: $\mu_{ii}^*(\omega_c) = \mu_{ij}^*(\omega_c) = 0$ [46–48, 50]. Within these approximations, the electron-boson coupling-constant matrix λ_{ij} becomes [46–48, 51]

$$\lambda_{ij} = \begin{pmatrix} 0 & 0 & \lambda_{13}^{sf} \\ 0 & 0 & \lambda_{23}^{sf} \\ \lambda_{31}^{sf} = \lambda_{13}^{sf} \nu_{13} & \lambda_{32}^{sf} = \lambda_{23}^{sf} \nu_{23} & 0 \end{pmatrix}, \quad (10)$$

where $\nu_{ij} = N_i(0)/N_j(0)$, and $N_i(0)$ is the normal density of states at the Fermi level for the i th band. The coupling constants λ_{ij}^{sf} are defined through the electron-antiferromagnetic spin fluctuation spectral functions (Eliashberg functions) $\alpha_{ij}^2 F_{ij}^{sf}(\Omega)$. Following Refs. [46–48] we choose these functions to have a Lorentzian shape, i.e.,

$$\alpha_{ij}^2 F_{ij}^{sf}(\Omega) = C_{ij} \{L(\Omega + \Omega_{ij}, Y_{ij}) - L(\Omega - \Omega_{ij}, Y_{ij})\}, \quad (11)$$

where

$$L(\Omega \pm \Omega_{ij}, Y_{ij}) = \frac{1}{(\Omega \pm \Omega_{ij})^2 + Y_{ij}^2}$$

and C_{ij} are normalization constants, necessary to obtain the proper values of λ_{ij} , while Ω_{ij} and Y_{ij} are the peak energies and the half-widths of the Lorentzian functions, respectively [46]. In all the calculations we set $\Omega_{ij} = \Omega_0$; i.e., we assume that the characteristic energy of spin fluctuations is the same for all the coupling channels, and $Y_{ij} = \Omega_0/2$, based on the results of inelastic neutron scattering measurements [52].

The peak energy of the Eliashberg functions, Ω_0 , can be directly associated to the experimental critical temperature, T_c , by using the empirical law $\Omega_0 = 2T_c/5 = 15.47$ meV that has been demonstrated to hold for iron pnictides [53]. We use a cutoff energy $\omega_c = 464$ meV and a maximum quasiparticle energy $\omega_{\max} = 619$ meV. The factors ν_{ij} that enter the definition of λ_{ij} (Eq. 10) can be extracted from the ARPES measurements [20] by assuming that the Fermi momentum in the i th band is proportional to the normal density of states at the Fermi level in the same band, i.e., $k_{Fi} \propto N_i(0)$. In this way, the ARPES results of Ref. [46] lead to $\nu_{12} = 2$, $\nu_{13} = 1$, and $\nu_{23} = 0.5$.

B. Calculation of the energy gaps and T_c

Now the model contains only two free parameters, i.e., λ_{13}^{sf} and λ_{23}^{sf} . To fix them, we initially solve the imaginary-axis Eliashberg equations [Eqs. (8) and (9)] to calculate the low-temperature values of the gaps, which are actually obtained by analytical continuation of the imaginary solutions to the real axis by using the technique of the Padé approximants. We find the values $\Delta_1 = 12.0$ meV, $\Delta_2 = 5.2$ meV, and $\Delta_3 = -12.0$ meV, that agree fairly well with the earlier experimental data quoted above, only when $\lambda_{13}^{sf} = 3.41$ and $\lambda_{23}^{sf} = 0.75$ for a total coupling $\lambda_{\text{tot}}^{sf} = 3.05$. Now that all the parameters of the model have been fixed, we can calculate the critical temperature, that turns out to be $T_c^* = 47.72$ K, much higher than the experimental one, $T_c = 38.7$ K, if the temperature where the London penetration depth diverges is considered. However, we should still take into account the *feedback* effect of the electronic condensate on the antiferromagnetic spin fluctuations [45, 46]. To this aim, we use the same input parameters as above, except for the electron-boson spectral functions that have an energy peak with the same temperature dependence of the superconductive gap [$\Omega_0(T) = \Omega_0 \tanh(1.76\sqrt{T_c^*/T - 1})$] [46]. Of course, at $T = T_c^*$ the energy peak is equal to zero, while at $T = 0$, the new spectral functions are equal to the old ones. In this way, the critical temperature calculated by solving the Eliashberg equations decreases to 38.7 K that corresponds exactly to the experimental one. Note that the total electron-boson coupling constant is $\lambda_{\text{tot}} = (\sum_{i,j=1}^3 N_i(0)\lambda_{ij}^{sf, ph})/(\sum_{i=1}^3 N_i(0)) = 3.05$ that is the signal of a strong coupling regime.

C. Calculation of the penetration depth

The penetration depth is another experimentally accessible physical quantity that can be also calculated within the three-band Eliashberg model, so as to further check the reliability of its predictions. The penetration depth of the magnetic field λ_L in the London limit [54], in a multiband model—without considering the anisotropy—is expressed as

$$\lambda_L^{-2}(T) = \left(\frac{\omega_p}{c}\right)^2 \sum_{i=1}^3 \left(\frac{\omega_{p,i}}{\omega_p}\right)^2 \pi T \times \sum_{n=-\infty}^{+\infty} \frac{\Delta_i^2(\omega_n) Z_i^2(\omega_n)}{[\omega_n^2 Z_i^2(\omega_n) + \Delta_i^2(\omega_n) Z_i^2(\omega_n)]^{3/2}}, \quad (12)$$

where c is the speed of light, and $Z_i(\omega_n)$ and $\Delta_i(\omega_n)$ are the solutions of the Eliashberg equations. The values of the single plasma frequencies $\omega_{p,i}$ for each band are not known. We assume that $\omega_{p,1} = \omega_{p,3}$ since the bands 1 and 3 are very similar to each other [20]. Thus, a best fit of the experimental data can be done with only two free parameters, $\frac{\omega_{p,1}^2}{\omega_p^2}$ and ω_p^2 .

IV. DISCUSSION AND CONCLUSIONS

A meaningful comparison between experimental and theoretical evaluations of λ_L can be made only once the effects of the penetration depth anisotropy are suitably taken into account. In fact, the material under investigation is known to show λ anisotropy, even if it is among the lowest for the iron pnictides. Thus, due to the adopted experimental configuration, the measured penetration depth is some combination of an in-plane component, $\lambda_{L,ab}$ (that in turn is assumed to be isotropic), and an out-of-plane component, $\lambda_{L,c}$. Also the calculations within the Eliashberg model were done in a completely isotropic approach. Therefore, in both cases corrections have to be done with the aim to compare only the in-plane components $\lambda_{L,ab}$. To do this, we consider, from the theoretical point of view, that $\lambda_{L,i}^2 \propto \omega_{p,i}^{-2}$ ($i = \text{total}, ab, c$) and that the total plasma frequency can be written as $\omega_p^2 = (2/3)\omega_{p,ab}^2 + (1/3)\omega_{p,c}^2$. Therefore, one can conclude here that

$$\lambda_{L,ab} = \lambda_L \left(\frac{2}{3} + \frac{1}{3\gamma_\lambda^2} \right)^{1/2} \quad (13)$$

where an anisotropy parameter $\gamma_\lambda = \lambda_{L,c}/\lambda_{L,ab}$ has been introduced.

On the other hand, from the experimental point of view, the measured penetration depth is a combination of the two components that depends on the sample geometry. Here we operate with the rf field parallel to the broad face of the crystal, i.e., parallel to the ab planes, and up to now we simply assumed that field penetration only occurs from the face parallel to the field. In this case, the fraction of the sample penetrated by the field is λ_L/c . However, due to the finiteness of the sample, the field penetrates also along the lateral sides. This was considered in literature only in the slab case, i.e., when a sample of constant cross section extends infinitely far in the direction of the applied field [55]. In such a case, the fraction of the volume penetrated by the field with respect to the total volume can be calculated, and in the limit of $\lambda_{L,ab} \ll c$ and $\lambda_{L,c} \ll b$ it reads [56] $\lambda_{L,ab}/c + \lambda_{L,c}/b$, where $2c$ and $2b$ are the dimensions of the sample perpendicular to the field. The problem is much more complex if the finiteness of the sample also in the direction of the field is taken into account, since large demagnetization effects occur and no closed form solutions of the London equation is available. It can be said that the penetration of the field occurs starting from all the sides of the crystal. Accordingly, and in the hypothesis that $\lambda_{L,ab} \ll c$ and $\lambda_{L,c} \ll a, b$, the fraction of penetrated volume can be estimated as $\lambda_{L,ab}/c + \lambda_{L,c}/a + \lambda_{L,c}/b$, to be compared to λ_L/c used above. Thus, the measured penetration depth can be expressed as

$$\lambda_L = \lambda_{L,ab} + \lambda_{L,c} \left(\frac{1}{a} + \frac{1}{b} \right) = \lambda_{L,ab} + \lambda_{L,c} f_s$$

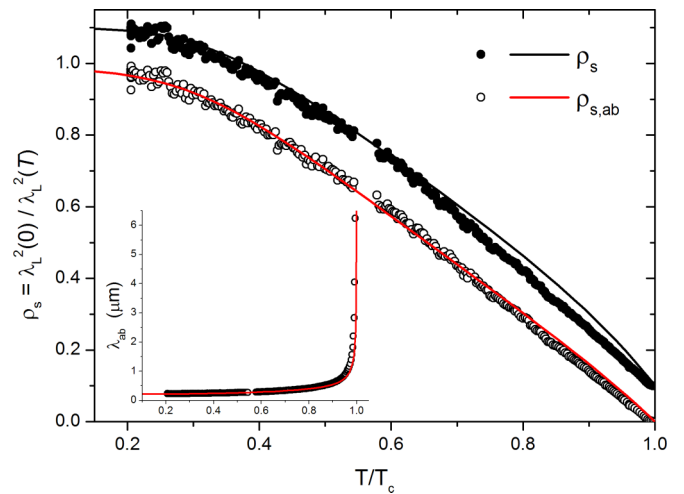


FIG. 6. Superfluid density as a function of the reduced temperature T/T_c , for calculated (lines) and experimental data (symbols). ρ_s was deduced as $\lambda_L^2(0)/\lambda_L^2(T)$ and is vertically shifted for clarity by 0.1, while $\rho_{s,ab}$ was calculated from the in-plane component of the penetration depth as $\lambda_{L,ab}^2(0)/\lambda_{L,ab}^2(T)$. The inset shows the absolute value of the in-plane $\lambda_{L,ab}$ as a function of T/T_c , for the experiment [symbols, see Eq. (14)] and for the model [line, see Eq. (13)].

where a shape factor, f_s , is defined. As a consequence,

$$\lambda_{L,ab} = \lambda_L (1 + \gamma_\lambda f_s)^{-1} \quad (14)$$

A deconvolution of the two components $\lambda_{L,ab}$ and $\lambda_{L,c}$ is possible in principle, by comparing results from samples with significantly different shape factors. This is not the present case, since the maximum variation of f_s for the analyzed crystals is about 30%. Thus, we consider $\gamma_\lambda(T)$ from literature. There is consensus on the decrease of γ_λ with temperature, but not on its absolute value [30,57]. We obtain the best results by assuming $\gamma_\lambda = 2 - T/T_c$, which is quite in agreement with ARPES results reported in Ref. [57].

Now the comparison between theory and experiment can be done. Figure 6 shows the superfluid density obtained from the experimental data and from the model calculation. ρ_s was deduced as $\lambda_L^2(0)/\lambda_L^2(T)$ (vertically shifted in the graph, for clarity). The best accordance, at low temperatures, was obtained by adjusting the only two free parameters in the calculation as $\frac{\omega_{p,1}^2}{\omega_p^2} = \frac{\omega_{p,3}^2}{\omega_p^2} = 0.1$ and $\omega_p = 1$ eV. Nevertheless, the accordance is not so good at temperatures approaching T_c . The agreement becomes remarkably good if only the in-plane component is considered, $\rho_{s,ab} = \lambda_{L,ab}^2(0)/\lambda_{L,ab}^2(T)$, where $\lambda_{L,ab}$ is deduced by Eqs. (13) and (14), for the model (red line) and the experiment (hollow symbols), respectively. Also the absolute values of the in-plane penetration depth agree very well, as shown in the inset. Figure 6 shows that experimental results and theoretical calculations are fully consistent. The low-temperature values, $\lambda_{L,ab}(5 \text{ K}) = 228$ nm from the experiment and $\lambda_{L,ab}(5 \text{ K}) = 224$ nm from the model, are also consistent with other literature findings [30].

In conclusion, we presented a novel experimental technique to characterize the high frequency properties of small superconducting samples, and we applied it to the study of high-quality optimally doped $\text{Ba}_{1-x}\text{K}_x\text{Fe}_2\text{As}_2$ single crystals.

The experimental penetration depth has been compared to the calculations based on the three-band Eliashberg equations within the $s \pm$ wave model. The model is intended to be simple enough to allow a practical comparison with experimental data, but still capturing the essential physics. The comparison has been made by considering the anisotropy of the penetration depth, and only two parameters in the calculation were left free in order to fit the experimental data. The agreement between theory and experiment is remarkable. The low-temperature values of the in-plane penetration depth [$\lambda_{L,ab}(5\text{ K}) = 228\text{ nm}$ for the experiment and $\lambda_{L,ab}(5\text{ K}) = 224\text{ nm}$ for the calculation] are also consistent with literature. Moreover, the value of the total plasma frequency here obtained (1.0 eV) is nicely close to that recently obtained by the analysis of optical data

(1.01 eV) [58]. This overall consistency validates the model itself, thus allowing us to set useful parameters that are missing in literature, such as the plasma frequency for each band: it turns out that $\omega_{p,1} = \omega_{p,3} = 0.32\text{ eV}$ and $\omega_{p,2} = 0.89\text{ eV}$. The higher value of the plasma frequency of band 2 with respect to bands 1 and 3 is consistent with the fact that the values of the coupling constants λ_1 and λ_3 are much larger than λ_2 , where $\lambda_i = \sum_{j=1}^3 \lambda_{ij}$, because the measured values are those of the bare $\omega_{p,i}$ renormalized by dividing by $1 + \lambda_i$ [59].

ACKNOWLEDGMENT

G.A.U. acknowledges support from the MEPHI (Russia) Academic Excellence Project (Contract No. 02.a03.21.0005).

-
- [1] K. Seo, B. A. Bernevig, and J. Hu, *Phys. Rev. Lett.* **101**, 206404 (2008).
- [2] G. R. Stewart, *Rev. Mod. Phys.* **83**, 1589 (2011).
- [3] A. S. Sefat, R. Jin, M. A. McGuire, B. C. Sales, D. J. Singh, and D. Mandrus, *Phys. Rev. Lett.* **101**, 117004 (2008).
- [4] C. Ren, Z.-S. Wang, H.-Q. Luo, H. Yang, L. Shan, and H.-H. Wen, *Phys. Rev. Lett.* **101**, 257006 (2008).
- [5] M. A. Tanatar, N. Ni, C. Martin, R. T. Gordon, H. Kim, V. G. Kogan, G. D. Samolyuk, S. L. Bud'ko, P. C. Canfield, and R. Prozorov, *Phys. Rev. B* **79**, 094507 (2009).
- [6] K. Hashimoto, T. Shibauchi, S. Kasahara, K. Ikada, S. Tonegawa, T. Kato, R. Okazaki, C. J. van der Beek, M. Konczykowski, H. Takeya, K. Hirata, T. Terashima, and Y. Matsuda, *Phys. Rev. Lett.* **102**, 207001 (2009).
- [7] L. Fang, Y. Jia, C. Chaparro, G. Sheet, H. Claus, M. A. Kirk, A. E. Koshelev, U. Welp, G. W. Crabtree, W. K. Kwok, S. Zhu, H. F. Hu, J. M. Zuo, H.-H. Wen, and B. Shen, *Appl. Phys. Lett.* **101**, 012601 (2012).
- [8] M. A. Tanatar, M. S. Torikachvili, A. Thaler, S. L. Bud'ko, P. C. Canfield, and R. Prozorov, *Phys. Rev. B* **90**, 104518 (2014).
- [9] Y. Liu, M. A. Tanatar, W. E. Straszheim, B. Jensen, K. W. Dennis, R. W. McCallum, V. G. Kogan, R. Prozorov, and T. A. Lograsso, *Phys. Rev. B* **89**, 134504 (2014).
- [10] B. Shen, M. Leroux, Y. L. Wang, X. Luo, V. K. Vlasko-Vlasov, A. E. Koshelev, Z. L. Xiao, U. Welp, W. K. Kwok, M. P. Smylie, A. Snezhko, and V. Metlushko, *Phys. Rev. B* **91**, 174512 (2015).
- [11] Z. Diao, D. Campanini, L. Fang, W.-K. Kwok, U. Welp, and A. Rydh, *Phys. Rev. B* **93**, 014509 (2016).
- [12] A. Yagil, Y. Lamhot, A. Almoalem, S. Kasahara, T. Watashige, T. Shibauchi, Y. Matsuda, and O. M. Auslaender, *Phys. Rev. B* **94**, 064510 (2016).
- [13] I. I. Mazin, D. J. Singh, M. D. Johannes, and M. H. Du, *Phys. Rev. Lett.* **101**, 057003 (2008).
- [14] A. V. Chubukov, D. V. Efremov, and I. Eremin, *Phys. Rev. B* **78**, 134512 (2008).
- [15] T. Saito, S. Onari, and H. Kontani, *Phys. Rev. B* **82**, 144510 (2010).
- [16] Y. Yamakawa and H. Kontani, *Phys. Rev. B* **92**, 045124 (2015).
- [17] Y. Bang and G. R. Stewart, *J. Phys.: Condens. Matter* **29**, 123003 (2017).
- [18] R. Prozorov, M. Konczykowski, M. A. Tanatar, A. Thaler, S. L. Budko, P. C. Canfield, V. Mishra, and P. J. Hirschfeld, *Phys. Rev. X* **4**, 041032 (2014).
- [19] A. E. Karakozov, S. Zapf, B. Gorshunov, Ya. G. Ponomarev, M. V. Magnitskaya, E. Zhukova, A. S. Prokhorov, V. B. Anzin, and S. Haindl, *Phys. Rev. B* **90**, 014506 (2014).
- [20] H. Ding, P. Richard, K. Nakayama, K. Sugawara, T. Arakane, Y. Sekiba, A. Takayama, S. Souma, T. Sato, T. Takahashi, Z. Wang, X. Dai, Z. Fang, G. F. Chen, J. L. Luo, and N. L. Wang, *Europhys. Lett.* **83**, 47001 (2008).
- [21] D.-H. Wu, W. L. Kennedy, C. Zahopoulos, and S. Sridhar, *Appl. Phys. Lett.* **55**, 696 (1989).
- [22] D. A. Bonn, D. C. Morgan, and W. N. Hardy, *Rev. Sci. Instrum.* **62**, 1819 (1991).
- [23] D. A. Bonn, P. Dosanjh, R. Liang, and W. N. Hardy, *Phys. Rev. Lett.* **68**, 2390 (1992).
- [24] T. Taen, F. Ohtake, H. Akiyama, H. Inoue, Y. Sun, S. Pyon, T. Tamegai, and H. Kitamura, *Phys. Rev. B* **88**, 224514 (2013).
- [25] G. Ghigo, F. Laviano, R. Gerbaldo, and L. Gozzelino, *Supercond. Sci. Technol.* **25**, 115007 (2012).
- [26] I. B. Vendik and O. G. Vendik, *High Temperature Superconductor Devices for Microwave Signal Processing—Part II* (Skalden, St. Petersburg, 1997).
- [27] G. Ghigo, R. Gerbaldo, L. Gozzelino, F. Laviano, and T. Tamegai, *IEEE Trans. Appl. Supercond.* **26**, 7300104 (2016).
- [28] W. N. Hardy, D. A. Bonn, D. C. Morgan, R. Liang, and K. Zhang, *Phys. Rev. Lett.* **70**, 3999 (1993).
- [29] D. A. Bonn, S. Kamal, K. Zhang, R. Liang, D. J. Baar, E. Klein, and W. N. Hardy, *Phys. Rev. B* **50**, 4051 (1994).
- [30] R. Prozorov and V. G. Kogan, *Rep. Prog. Phys.* **74**, 124505 (2011).
- [31] U. Welp, R. Xie, A. E. Koshelev, W. K. Kwok, H. Q. Luo, Z. S. Wang, G. Mu, and H. H. Wen, *Phys. Rev. B* **79**, 094505 (2009).
- [32] H. Ding, K. Nakayama, P. Richard, S. Souma, T. Sato, T. Takahashi, M. Neupane, Y.-M. Xu, Z.-H. Pan, A. V. Fedorov, Z. Wang, X. Dai, Z. Fang, G. F. Chen, J. L. Luo, and N. L. Wang, *J. Phys.: Condens. Matter* **23**, 135701 (2011).
- [33] I. Vendik, *Supercond. Sci. Technol.* **13**, 974 (2000).
- [34] K. Nakayama, T. Sato, P. Richard, Y.-M. Xu, T. Kawahara, K. Umezawa, T. Qian, M. Neupane, G. F. Chen, H. Ding, and T. Takahashi, *Phys. Rev. B* **83**, 020501 (2011).
- [35] Y.-M. Xu, Y.-B. Huang, X.-Y. Cui, E. Razzoli, M. Radovic, M. Shi, G.-F. Chen, P. Zheng, N.-L. Zhang, C.-L. Zhang, P.-C. Dai, J.-P. Hu, Z. Wang, and H. Ding, *Nat. Phys.* **7**, 198 (2011).
- [36] D. S. Inosov, J. T. Park, A. Charnukha, Y. Li, A. V. Boris, B. Keimer, and V. Hinkov, *Phys. Rev. B* **83**, 214520 (2011).

- [37] L. Wray, D. Qian, D. Hsieh, Y. Xia, L. Li, J. G. Checkelsky, A. Pasupathy, K. K. Gomes, C. V. Parker, A. V. Fedorov, G. F. Chen, J. L. Luo, A. Yazdani, N. P. Ong, N. L. Wang, and M. Z. Hasan, *Phys. Rev. B* **78**, 184508 (2008).
- [38] K. Nakayama, T. Sato, P. Richard, Y.-M. Xu, Y. Sekiba, S. Souma, G. F. Chen, J. L. Luo, N. L. Wang, H. Ding, and T. Takahashi, *Europhys. Lett.* **85**, 67002 (2009).
- [39] G. Mu, H. Luo, Z. Wang, L. Shan, C. Ren, and H. H. Wen, *Phys. Rev. B* **79**, 174501 (2009).
- [40] F. Y. Wei, B. Lv, Y. Y. Xue, and C. W. Chu, *Phys. Rev. B* **84**, 064508 (2011).
- [41] J. G. Storey, J. W. Loram, J. R. Cooper, Z. Bukowski, and J. Karpinski, *Phys. Rev. B* **88**, 144502 (2013).
- [42] P. Popovich, A. V. Boris, O. V. Dolgov, A. A. Golubov, D. L. Sun, C. T. Lin, R. K. Kremer, and B. Keimer, *Phys. Rev. Lett.* **105**, 027003 (2010).
- [43] K. Matano, Z. Li, G. L. Sun, D. L. Sun, C. T. Lin, M. Ichioka, and G.-Q. Zheng, *Europhys. Lett.* **87**, 27012 (2009).
- [44] G. M. Eliashberg, *Sov. Phys. JETP* **11**, 696 (1960).
- [45] A. V. Chubukov, D. Pines, and J. Schmalian, in *Superconductivity Vol. 2: Novel Superconductors*, edited by K. H. Bennemann and J. B. Ketterson (Springer-Verlag, Berlin, 2008); D. Manske, I. Eremin, and K. H. Bennemann, in *Superconductivity Vol. 2: Novel Superconductors*, edited by K. H. Bennemann and J. B. Ketterson (Springer-Verlag, Berlin, 2008).
- [46] G. A. Ummarino, *Phys. Rev. B* **83**, 092508 (2011).
- [47] G. A. Ummarino, M. Tortello, D. Daghero, and R. S. Gonnelli, *Phys. Rev. B* **80**, 172503 (2009).
- [48] G. A. Ummarino, M. Tortello, D. Daghero, and R. S. Gonnelli, *J. Supercond. Nov. Magn.* **24**, 247 (2011).
- [49] L. Boeri, M. Calandra, I. I. Mazin, O. V. Dolgov, and F. Mauri, *Phys. Rev. B* **82**, 020506 (2010).
- [50] P. J. Hirschfeld, M. M. Korshunov, and I. I. Mazin, *Rep. Prog. Phys.* **74**, 124508 (2011).
- [51] I. I. Mazin and J. Schmalian, *Physica C* **469**, 614 (2009).
- [52] D. S. Inosov, J. T. Park, P. Bourges, D. L. Sun, Y. Sidis, A. Schneidewind, K. Hradil, D. Haug, C. T. Lin, B. Keimer, and V. Hinkov, *Nat. Phys.* **6**, 178 (2010).
- [53] J. Paglione and R. L. Greene, *Nat. Phys.* **6**, 645 (2010).
- [54] A. A. Golubov, A. Brinkman, O. V. Dolgov, J. Kortus, and O. Jepsen, *Phys. Rev. B* **66**, 054524 (2002).
- [55] P. A. Mansky, P. M. Chaikin, and R. C. Haddon, *Phys. Rev. B* **50**, 15929 (1994).
- [56] J. D. Fletcher, A. Carrington, P. Diener, P. Rodiere, J. P. Brison, R. Prozorov, T. Olheiser, and R. W. Giannetta, *Phys. Rev. Lett.* **98**, 057003 (2007).
- [57] R. Khasanov, D. V. Evtushinsky, A. Amato, H.-H. Klauss, H. Luetkens, C. Niedermayer, B. Buchner, G. L. Sun, C. T. Lin, J. T. Park, D. S. Inosov, and V. Hinkov, *Phys. Rev. Lett.* **102**, 187005 (2009).
- [58] J. Hwang, *J. Phys.: Condens. Matter* **28**, 125702 (2016).
- [59] S.-L. Drechsler, H. Rosner, V. Grinenko, and S. Johnston, [arXiv:1701.00596](https://arxiv.org/abs/1701.00596).